Research in Astron. Astrophys. **2009** Vol. **9** No. **3**, 333–340
http://www.raa-journal.org *http://www.iop.org/journals/raa*

***R**esearch in*
***A**stronomy and*
***A**strophysics*

A super-high angular resolution principle for coded-mask X-ray imaging beyond the diffraction limit of a single pinhole *

Chen Zhang[1] and Shuang-Nan Zhang[2,3]

[1] Department of Engineering Physics & Center for Astrophysics, Tsinghua University, Beijing 100084, China; *zhangchen12@gmail.com*
[2] Key Laboratory of Particle Astrophysics, Institute of High Energy Physics, the Chinese Academy of Sciences, Beijing 100049, China
[3] Department of Physics & Center for Astrophysics, Tsinghua University, Beijing 100084, China; *zhangsn@tsinghua.edu.cn*

Received 2008 May 5; accepted 2008 June 4

Abstract High angular resolution X-ray imaging is always useful in astrophysics and solar physics. In principle, it can be performed by using coded-mask imaging with a very long mask-detector distance. Previously, the diffraction-interference effect was thought to degrade coded-mask imaging performance dramatically at the low energy end with its very long mask-detector distance. The diffraction-interference effect is described with numerical calculations, and the diffraction-interference cross correlation reconstruction method (DICC) is developed in order to overcome the imaging performance degradation. Based on the DICC, a super-high angular resolution principle (SHARP) for coded-mask X-ray imaging is proposed. The feasibility of coded mask imaging beyond the diffraction limit of a single pinhole is demonstrated with simulations. With the specification that the mask element size is $50 \times 50\ \mu\mathrm{m}^2$ and the mask-detector distance is 50 m, the achieved angular resolution is 0.32 arcsec above about 10 keV and 0.36 arcsec at 1.24 keV ($\lambda = 1$ nm), where diffraction cannot be neglected. The on-axis source location accuracy is better than 0.02 arcsec. Potential applications for solar observations and wide-field X-ray monitors are also briefly discussed.

Key words: instrumentation: high angular resolution — techniques: image processing — telescopes

1 INTRODUCTION

High angular resolution X-ray imaging is always useful in astrophysics and solar physics, for example to study black holes near their event horizons, relativistic jets of super massive black holes, as well as solar flares and coronal activities. So far, the best imaging technology for X-ray observation is performed by grazing incidence reflection (Aschenbach 1985), which provides very good angular resolution, for example, down to 0.5 arcsec, as in the case of the Chandra X-ray Observatory (Weisskopf et al. 2000). The diffraction limit of Chandra is about 8 miliarcsec at 6 keV; however, slope errors and other surface irregularities that affect the angle of reflection prevent an angular resolution better than 0.5 arcsec. Furthermore, the grazing incidence reflection is limited by the working energy band, which hardly exceeds tens of keV. A possible way to improve the angular resolution beyond that of Chandra requires a

* Supported by the National Natural Science Foundation of China.

different technology, for example the diffractive-refractive X-ray optics proposed by Gorenstein (2007) or the Fourier-Transform imaging by Prince et al. (1988). As an alternative, the concept of a super-high angular resolution principle (SHARP) for a coded-mask X-ray imaging telescope is proposed here.

The coded mask imaging technology, which has been reviewed by Zand (1996), has been widely applied for X-ray observations, for example the INTEGRAL mission (Winkler et al. 2003) of ESA and the SWIFT mission (Gehrels 2004) of NASA. Both missions have angular resolutions in the tens of arcmin, since the distances between the masks and the detectors are limited by the dimensions of the satellites. In principle, super-high angular resolution better than Chandra can be achieved by a coded-mask telescope with sub-millimeter size of mask pinholes and long mask-detector distances, which can be tens or even hundreds of meters long with the formation-flying technology (for example proposed for XEUS (ESA 2001) of ESA) or the mast technology (for example applied in the Polar mission of NASA). The X-ray diffraction effect in a coded-mask system has been commonly thought to be negligible due to high photon energies in the hard X-ray and gamma-ray range as well as relatively small mask-detector distance. Whereas for a coded-mask telescope with a super high angular resolution in the milli-arc-second range, the X-ray diffraction effect could not be neglected, especially at the low energy end (in the range of several keV), which might markedly degrade the imaging performance, as pointed out by Prince et al. (1988) and Skinner (2004). In this work, we study the diffraction effect in SHARP with numerical computations, and propose a diffraction-interference cross correlation reconstruction method and demonstrate the feasibility of coded mask imaging beyond the diffraction limit of a single pinhole. A potential application for solar observations is also briefly discussed.

2 THE CODED-MASK PRINCIPLE AND DIFFRACTION-INTERFERENCE RECONSTRUCTION

2.1 The Coded-mask Principle and SHARP

In the limit of geometrical optics, i.e., the diffraction effect is not considered, the basic concept of coded-mask imaging is shown in Figure 1. The coded-mask camera has a mask on top of a position-sensitive detector with a mask-detector distance D. Two point sources project the mask pattern onto the detector plane. The shift and the strength of projections separately encode the positions and the fluxes of observed sources. The detection of the X-ray flux can be described with Equation (1) (Fenimore et al. 1978),

$$P = O * M + N_{\rm noise}, \tag{1}$$

where O is the X-ray flux spatial distribution, M is the encoding pattern of the mask and $*$ means cross correlation. For the commonly applied cross correlation method, a matrix G is used for reconstruction, as shown in Equation (2),

$$O' = P * G = O * (M * G) + N_{\rm noise} * G, \tag{2}$$

where O' is the estimation of the X-ray flux spatial distribution, if $M * G$ is a δ function. The encoding pattern M is often chosen so that its auto-correlation function is a δ function. Therefore $G = M$ is commonly applied. The width of the Point Spread Function (PSF) obtained with Equation (2) is defined as $\Delta_i = \frac{d_{\rm m}}{D}$ ($d_{\rm m}$ is the size of the mask element). The cyclic optimal coded-mask configuration (Zand 1996) is also employed here. The coded mask or the mask pattern, which consists of four basic patterns, is about four times the size of the detector, and one basic pattern cyclically extends about twice along the width and length directions of the mask. In the next sections, simulations are done with the following assumptions: the basic pattern is totally random; the detector pixel size is equal to the mask element size, both of which have square shapes; the mask and the detector are assumed to be idealized, i.e., the mask has no thickness, the opaque mask elements block the X-rays completely and one incident event can only be recorded in one detector pixel.

In this work, $d_{\rm m} = 50 \times 10^{-6}\,{\rm m}$ and $D = 50\ {\rm m}$ are chosen to be the basic parameters for the simulations of SHARP, which means $\Delta_i = 0.2\,{\rm arcsec}$ in the sub-arcsec range. Since the simulations employ a two dimensional FFT (please refer to Section 2.2) which requires tremendous computing

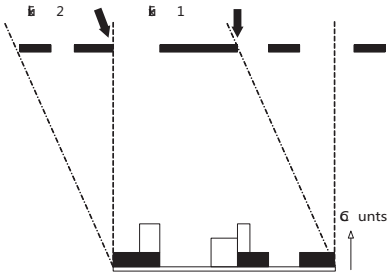

Fig. 1 Basic concept of coded-mask imaging, in the limit of geometrical optics, i.e., the diffraction effect is negligible. Two point sources illuminate a position-sensitive detector plane through a mask made of many square pinholes. The detector plane thus records two projections of the mask pattern. The shift and the strength of projections separately encode the positions and the fluxes of the sources. The PSF width is defined as $\Delta_i = \frac{d_{\rm m}}{D}$.

resources, the basic simulated pattern contains only 200×200 elements, i.e., the reconstructed image contains the same pixels and each pixel is $0.2 \times 0.2\ \mathrm{arcsec}^2$. The fully coded Field-Of-View (FOV) is $40 \times 40\ \mathrm{arcsec}^2$.

2.2 The Diffraction-Interference Cross Correlation Method

As shown in Figure 2, A is the mask modulation function, which is 1 or 0 with an idealized mask. $\boldsymbol{r}$ is a vector from point (x_0, y_0) on the mask to (x, y) on the detector. $\boldsymbol{k}$ is the wave vector. Since there are many pinholes in the mask, both diffraction and interference will take place on the detector plane. The diffraction-interference is described with the Fresnel-Huygens principle (Lindsey 1978) as,

$$E_R(x, y) = C \int_{\infty}^{\infty} \int_{\infty}^{\infty} E_i(x_0, y_0) A(x_0, y_0) \frac{e^{ikr}}{r} dx_0 dy_0, \tag{3}$$

where E_i is the amplitude distribution of incident photons, which is described with the plane wave in our case as $E_i = A_i * e^{i\boldsymbol{k}\,\cdot\,\boldsymbol{r}}$. The flux distribution is proportional to E_i^2. $C = -i/\lambda$ is constant. In our case, the dimension of the mask is far less than the mask-detector distance D, so we have $r \simeq D + \frac{x^2+x_0^2+y^2+y_0^2-2xx_0-2yy_0}{2D}$. Therefore Equation (3) becomes

$$E_R(x, y) = C_2 \int_{\infty}^{\infty} \int_{\infty}^{\infty} M e^{-2i\pi(f_x x_0 + f_y y_0)} dx_0 dy_0, \tag{4}$$

where $C_2 = \frac{-i}{\lambda D} e^{ikD} e^{\frac{ik}{2D}(x^2+y^2)}$, $f_x = x/\lambda D$, $f_y = y/\lambda D$, $M = E_i(x_0, y_0) A(x_0, y_0) e^{\frac{ik}{2D}(x_0^2+y_0^2)}$. Equation (4) is the Fourier transform approximation of the Fresnel-Huygens principle, which can be simulated with an FFT algorithm. The conditions for the validity of this approximation are discussed by Lindsey (1978), and are satisfied in our simulations.

The X-ray diffraction cannot be neglected at the low energy end as in Figure 3, which shows the simulated flux distribution on the detector plane with a $50\ \mu\mathrm{m}$ square pinhole in front of it (50 m away) for 1.24 keV photons (corresponding to X-ray's wavelength of $\lambda = 1$ nm). The flux spreads much larger than $50\ \mu\mathrm{m}$ (each pixel in Fig. 3 is $50 \times 50\ \mu\mathrm{m}^2$) due to the diffraction effect.

If the reconstruction matrix G in the cross correlation method is still chosen to be equal to M (a so-called geometrical reconstruction matrix, which is indicated as G_O) at the low energy end, the diffraction effect would markedly degrade the reconstructed image. Figure 4a shows the reconstructed image of a monochromatic on-axis point source ($\lambda = 1$ nm) obtained by the geometrical matrix. The reconstructed image is normalized so that the total integral flux is one photon, and all the reconstructed images in this work are normalized in the same way, unless otherwise specified. The point source is hardly identified with the Fresnel diffraction stripes clearly observed. Since the X-ray probability waves through different

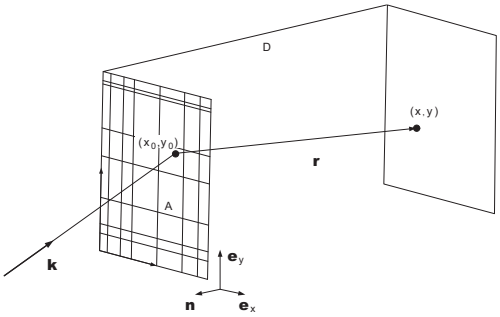

Fig. 2 Monochromatic X-ray with wave vector $\boldsymbol{k}$ illuminating a mask in the x_0-y_0 plane produces a diffraction pattern in the $x - y$ plane (Lindsey 1978).

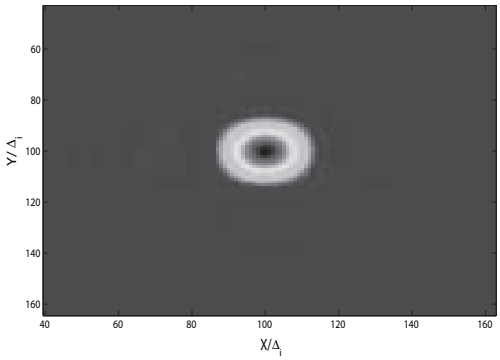

Fig. 3 Simulated flux distribution on the detector plane for 1.24 keV photons ($\lambda = 1$ nm) with a $50\ \mu$m square pinhole in front of it (50 m away). The flux spread is much larger than $50\ \mu$m caused by diffraction as one pixel is $50 \times 50\ \mu\mathrm{m}^2$. Therefore this diffraction effect must be included when reconstructing the image of the incoming X-ray with the cross-correlation effect.

mask open elements interfere with each other, the mask spatial information should be encoded into the diffraction-interference pattern on the detector. We then choose the reconstruction matrix G at certain energy as the normal incident diffraction-interference pattern (so-called diffraction-interference matrix, which is indicated as G_{DI}) on the detector plane. Figure 4b shows the reconstructed image obtained with G_{DI} of the same source in Figure 4a, and the point source can be clearly identified although slight Fresnel stripes still exist. This new reconstruction method is called a diffraction-interference cross correlation method (DICC), which can be described with Equation (5),

$$O' = P * G_{\mathrm{DI}} = O * (M * G_{\mathrm{DI}}) + N_{\mathrm{noise}} * G_{\mathrm{DI}}. \tag{5}$$

G_{DI} can be obtained by numerical simulation as shown in Equation (4) or from actual measurements. The angular resolution of DICC is beyond the single pinhole (the single mask open element) diffraction limit as indicated in Figure 4.

3 THE SIMULATION RESULTS

We have simulated the reconstructed images at several energies from 1.24 keV ($\lambda = 1$ nm) to 6.2 keV ($\lambda = 0.2$ nm), where DICC is valid. To illustrate the main properties of this method, we mainly discuss the imaging performance of DICC around 1 nm, which is also compared with that in the limit of geometrical optics.

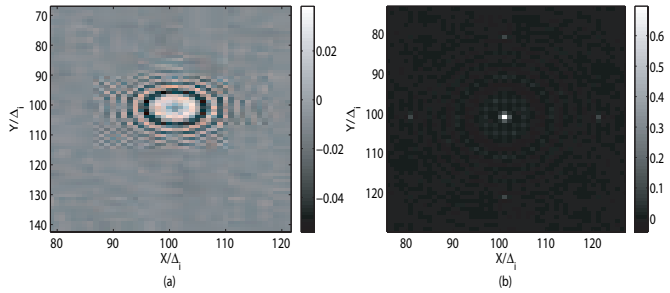

Fig. 4 Reconstructed images of a monochromatic ($\lambda = 1$ nm) on-axis point source: (a) the cross-correlation with the G_O, the diffraction degrades the reconstruction dramatically, because the diffraction pattern shown in Fig. 3 has not been taken into consideration; (b) with DICC, the point source can be clearly identified although slight Fresnel diffraction stripes still exist. The DICC can thus largely overcome the degradation of the imaging performance due to the diffraction of each pinhole.

3.1 Angular Resolution

We calculate the reconstructed image of two point sources with the same flux (Poisson fluctuations are not considered here). The angular resolution is defined as the minimum angular distance between these two sources, which can be separated by the 50% contour line of the maximum flux on the reconstructed image. Figure 5a shows the reconstructed images in the limit of geometrical optics for two point sources with angular distance $1.5\Delta_i = 0.3$ arcsec; the two sources cannot be separated. However in Figure 5b, two sources with angular distance $1.6\Delta_i = 0.32$ arcsec can just be separated. Therefore, the angular resolution is 0.32 arcsec in the limit of geometrical optics, i.e., at the high energy end (above about 10 keV) where diffraction is negligible. With the same procedure, the angular resolution of DICC for $\lambda = 1$ nm photons is obtained as 0.36 arcsec, i.e., the two sources cannot be separated in Figure 5c, but can be separated in Figure 5d. This means the diffraction effect degrades the angular resolution by only about 12.5%, a significant improvement as compared to that in Figure 3. We also calculated the reconstructed images with DICC for $\lambda = 1$ nm point sources at different locations inside the FOV, but no observable reconstruction degradation is found compared with the on-axis source case.

3.2 Source Location Accuracy

The reconstructed images for an on-axis point source are simulated 10000 times with 1000 photons recorded (Poisson fluctuations are considered). The source location of each simulation is calculated by fitting the reconstructed image to the PSF. The calculated source location distribution with DICC for $\lambda = 1$ nm is shown in Figure 6a, which is concentrated within $0.1\Delta_i = 0.02$ arcsec. The same simulation is also done in the limit of geometrical optics, which is shown in Figure 6b. Therefore, the source location accuracy is better than $0.1\Delta_i = 0.02$ arcsec for 1000 detected photons.

3.3 System Constraints

Since the diffraction pattern on the detector plane is energy dependent, the diffraction matrix G is also energy dependent. In practice, the detector cannot identify two photons with an energy difference within the detector's spectroscopy resolution, i.e., in practice photons within a small energy band must share a common diffraction matrix. Figure 7 shows the reconstructed images of several on-axis point sources with wavelengths around 1 nm, which all apply the diffraction matrix of 1 nm photons (marked as G_1). The point source can be clearly identified. Obviously, the imaging qualities are degraded by applying G_1 instead of their own diffraction matrixes. Table 1 gives the angular resolution at several wavelengths around 1 nm by applying G_1 as the reconstruction matrix instead of their own. For the 1.05 nm on-axis source, the angular resolution is degraded to $2.05\Delta_i = 0.41$ arcsec by applying G_1.

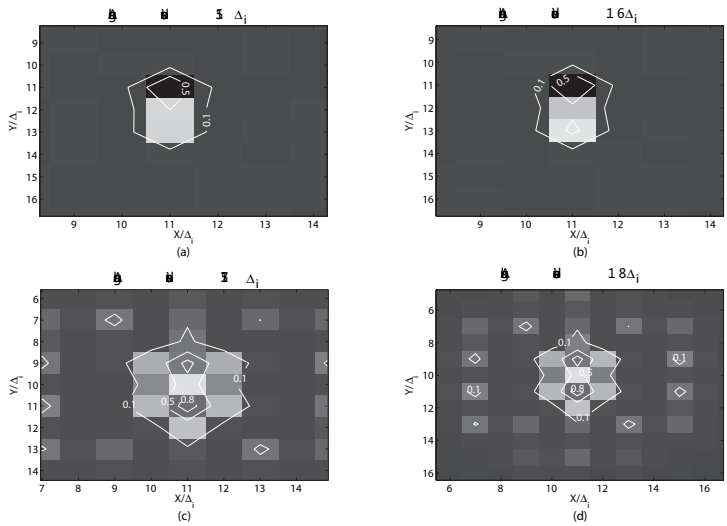

Fig. 5 Angular resolution of the simulated system: (a) and (b) are in the limit of geometrical optics; (c) and (d) are obtained with DICC for $\lambda = 1$ nm sources. In (a) and (c), two sources cannot be separated. However in (b) and (d), two sources can be separated. The angular resolution is 0.32 arcsec in the limit of geometrical optics and is degraded to 0.36 arcsec for $\lambda = 1$ nm sources.

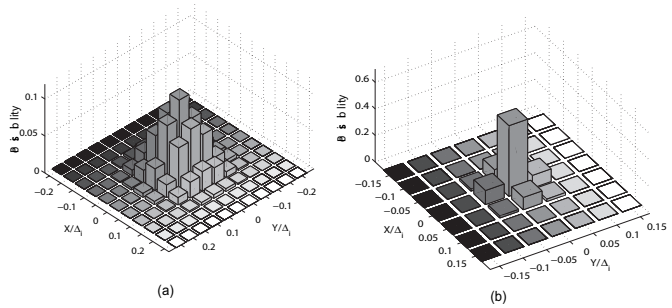

Fig. 6 Calculated source location distribution of the reconstructed images for an on-axis point source, which is simulated 10000 times with 1000 photons recorded: (a) with DICC for $\lambda = 1$ nm photons; (b) in the limit of geometrical optics. The source location accuracy is better than $0.1\Delta_i = 0.02$ arcsec.

Table 1 Degradation of the Angular Resolution with a Shared Reconstruction Matrix

Wavelength (nm)	0.95	0.97	0.99	1	1.01	1.03	1.05
Angular resolution (arcsec)	0.39	0.38	0.37	0.36	0.37	0.39	0.41

Based on the detector energy resolution, the system constraint is considered. Assuming the detector pixel size d_d, the difference δd of the main diffraction stripe diameters of photons with wavelength difference $\delta\lambda$ is

$$\delta d = \frac{\delta\lambda * D}{d_{\mathrm{m}}}. \tag{6}$$

If the spectroscopic resolution of the detector is $\delta\lambda$, spatially the detector does not need to distinguish δd for photons with wavelength difference $\delta\lambda$,

$$\delta d \leq f * d_d. \tag{7}$$

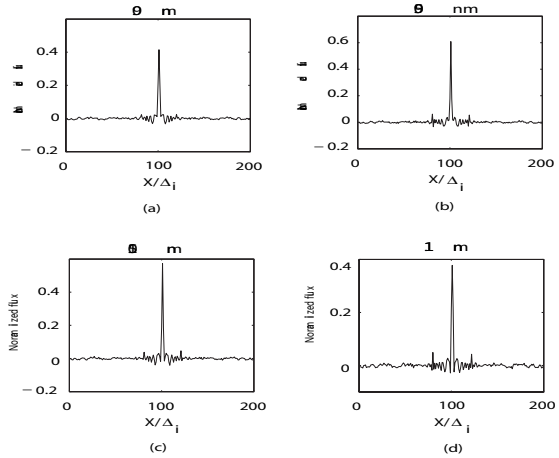

Fig. 7 Reconstructed images of (a) 0.9 nm (b) 0.95 nm (c) 1.05 nm and (d) 1.1 nm photons, which all apply the same diffraction-interference matrix G_1 (the diffraction-interference matrix of 1 nm photons).

Table 2 Comparison between SHARP and Several Missions

Mission	SHARP	Chandra	Integral[a]	RHESSI	Hinode (Solar B)[b]
Imaging technology	Coded-mask	Focusing	Coded-mask	Rotation Modulation & Fourier Transform	Focusing
Energy band	1–100 keV	Up to 10 keV	15 keV–10 MeV	3–150 keV[c]	About to 6 keV
Energy resolution	133 eV@5.9 keV[d]	ACIS: about 148 eV@5.9 keV[e]	9 % @ 100 keV	<1 keV[f]	$<$280 eV @5.9 keV[g]
Angular resolution	0.32–0.36 arcsec	0.5 arcsec[h]	12 arcmin	2.26 arcsec[i]	2 arcsec @ 0.523 keV[j]

a: IBIS onboard; b: XRT onboard; c: The upper layer; d: Take DEPFET as focal plane detector (Treis et al. 2006); e: CCD S3 on board; f: Below 100 keV; g: Calculated based on the ENC $<$ 30 el; h: On-axis point source; i: The collimator #1; j: 68% source flux within 2 arcsec.

Here, $f \geq 1$ is a constant and depends upon the mask open fraction. For a 50% open mask, our simulations indicate that $1 \leq f \leq 2$. For a mask fraction much less than 50%, $f > 2$ is possible. Then with known basic parameters, i.e., $d_{\rm m}$ and D, the requirement for detector spectroscopic resolution is

$$\delta\lambda \leq f * \Delta_i * d_d. \tag{8}$$

In practice, $d_{\rm m}$ and D are chosen to match the detector performance, which means

$$d_{\rm m} \geq \frac{\delta\lambda}{f * \Delta_i}, \tag{9}$$

or

$$D = \frac{d_{\rm m}}{\Delta_i} \leq \frac{d_d}{\Delta_i} \leq \frac{\delta\lambda}{(\Delta_i)^2 f}. \tag{10}$$

Therefore, the larger the f is, the more compact the system can be. Here $f = 1$ is chosen for convenience, with which $\delta\lambda = 0.05$ nm, $d_{\rm m} = 50\ \mu$m and $D = 50$ m satisfies the system constraint. The spectroscopic resolution of 0.05 nm requires about a 120 eV energy resolution at $\lambda = 1$ nm, which can be provided by modern silicon imaging detectors like CCDs or DEPFETs (Strüder 2000).

4 DISCUSSION AND CONCLUSIONS

By applying DICC, the angular resolution of coded-mask imaging system is no longer limited by the single pinhole diffraction limit at the low energy end, but rather limited by detector spectroscopy performance. Table 2 shows a brief comparison of SHARP with several X-ray astronomy missions. The advantage of SHARP is quite obvious: excellent angular resolution and an easily fabricated mask which does not require high accuracy in mechanical fabrication of X-ray grazing lens. However, the detector's effective area of a coded-mask telescope is smaller than its actual area due to the encoding pattern. Furthermore, each detector pixel receives background photons from all over the FOV. Therefore, the sensitivity is limited by its large background and small effective area compared with that in the grazing incidence reflection case.

Current detector technology can provide even better energy resolution than 0.05 nm at 1 nm, which means the angular resolution discussed above can be improved further by increasing the mask-detector distance D as indicated in Equation (10) or by decreasing the mask element size as indicated in Equation (9). For example, for a detector with 0.002 nm spectroscopic resolution (5 eV at 1 keV), $d_{\rm m} = 1$ or $40\ \mu{\rm m}$ and $D = 20$ or 800 m satisfies the system constraint with $\Delta_i = 0.01\ {\rm arcsec}$.

A potential application of SHARP will be the solar observation in the 1–100 keV energy band with sub-arcsec angular resolution. The main objectives may be the coronal mass ejection (CME) and solar flares, which include fine structures and evolutions of the solar flares, nonlinear solar flare dynamics, a solar particle acceleration mechanism etc. Therefore, applications of SHARP are foreseen to make significant progress in the study of solar high energy explosive events and space weather forecast modeling. Another potential application is to make wide-field X-ray monitors with SHARP; its sub-arcsec angular resolution may allow the counterparts of gamma-ray bursts, X-ray bursts and black hole and neutron star transients to be identified without the requirement of subsequent follow-up observations of focusing X-ray telescopes.

Acknowledgements We thank C. Fang, W. Q. Gan, J. Y. Hu, Z. G. Dai, X. D. Li, Y. F. Huang and X. Y. Wang for many interesting discussions and suggestions on SHARP and its potential applications. We are grateful to the anonymous referee for promptly providing valuable comments and suggestions. SNZ acknowledges partial funding support by the Ministry of Education of China, Directional Research Project of the Chinese Academy of Sciences under project No. KJCX2-YW-T03 and by the National Natural Science Foundation of China under grant Nos. 10521001, 10733010, 10725313 and 10327301.

References

Aschenbach, B. 1985, Reports on Progress in Physics, 48, 579
Fenimore, E. E., & Cannon, T. M. 1978, Applied Optics, 17, 337
Gehrels, N. 2004, New Astronomy Reviews, 48, 431
Gorenstein, P. 2007, Advances in Space Research, 40, 1276
Lindsey, C. A. 1978, J. Opt. Soc. Am., 68, 1708
Prince, T. A., Hurford, G. J., Hudson, H. S., & Crannell, C. J. 1988, Solar Phys., 118, 269
Skinner, G. K. 2004, New Astronomy Reviews, 48, 205
Strüder, L. 2000, Nucl. Instr. and Meth. A, 454, 73
The XEUS Telescope Working Group, 2001, X-ray evolving universe spectroscopy-the XEUS telescope, ESA SP-1253
Treis, J., Fischer, P., Halker, O., et al. 2006, Nucl. Instr. and Meth. A, 568, 191
Weisskopf, M. C., Tananbaum, H. D., Van Speybroeck, L. P., et al. 2000, In: J. Truemper, B. Aschenbach, eds., Proceedings of SPIE, 4012, 2
Winkler, C., Courvoisier, T. J.-L., Cocco, G. D., et al. 2003, A&A, 411, L1
Zand, J. 1996, Coded aperture camera imaging concept [EB/OL], *http://lheawww.gsfc.nasa.gov/docs/cai/coded.html*